

Noise Source Location Techniques – Simple to Advanced Applications

Mehdi Batel and Marc Marroquin, Brüel & Kjær North America, Inc., Norcross, Georgia

Jørgen Hald, Jacob J. Christensen, Andreas P. Schuhmacher and Torben G. Nielsen, Brüel & Kjær, Denmark

There are several noise source location techniques available to engineers working on Noise, Vibration and Harshness (NVH) problems. Choosing the right technique depends on the application, as well as the information required. This article reviews techniques for noise source location and quantification applications, including the relatively new beamforming method. An innovative beamformer microphone array is also presented and compared to traditional array designs and performances.

Modern noise source location techniques are extremely valuable tools in mechanical engineering industries. It is important to understand the acoustic behavior of structures in the automotive and aerospace industries, as noise investigations are crucial for regulations and research and development. Furthermore, it is important to be able to locate and quantify noise sources with reliable, fast and accurate techniques. Due to the excellent performance of modern computers and advances in acoustics sciences, many new tools are available that can be used by any NVH engineer.

This article presents a review of the following noise source location techniques:

- Sound pressure mapping.
- Sound intensity and selective intensity.
- Near-field acoustic holography.
- Non-stationary acoustic holography.
- Beamforming (phased array technique).
- Inverse Boundary Element Methods (IBEM).

Sound Pressure Level Measurements

The simplest method for detecting noise sources is by measuring the Sound Pressure Level (SPL) at various locations surrounding a noisy product. The SPL can be measured by a single channel FFT or 1/3 octave analyzer. At each point of a defined grid, the analyzer will perform an average of the different time samples for a defined averaging time, then calculate a spectrum of the sound pressure level at that particular location. By utilizing all the measured SPLs, one can present the data on a contour map (iso-pressure representation) and gain some rough idea of the location of a sound source and its characteristics.

The measured sound pressure level in this case is defined as:^{1,2}

$$L_p = 10 \log_{10} \left(\frac{(p^2)_{av}}{p_{ref}^2} \right) \quad (1)$$

where $(p^2)_{av}$ is the mean squared pressure and p_{ref} is the reference pressure, equal to 2×10^{-5} Pa for airborne sounds.

Benefits:

- Low equipment cost.
- Easy measurement technique.
- The frequency limitation is based on the microphones or the analyzer.

Limitations:

- Time consuming.
- Scalar based technique, no determination of sound direction or acoustic directional fluctuations.
- Measurements cannot be performed in the near-field.
- Sound pressure measured is a summation of the actual sound

source plus many other acoustic contributions (reflections, background noise, etc.).

- Measurements are only relevant on stationary sources.

Sound Intensity Techniques

Sound intensity is a well-known application that measures acoustic energy flow and provides information about sound amplitude and direction in the acoustic field. Figure 1 shows a typical sound intensity probe that uses a face-to-face microphone design. Since sound intensity is determined from the phase difference of the two sound pressure levels measured by the microphones, a phase matching needs to be performed on the probe as well as on the data acquisition system. A precise phase matching can be performed by integral microphone phase-corrector units (patented) that are fitted into the microphones.

The average measured pressure is calculated by the following formula:

$$p = \frac{P_1 + P_2}{2} \quad (2)$$

The instantaneous particle velocity is then calculated using the one-dimensional thermodynamic Euler's equation:

$$v = -\frac{1}{\rho} \int \frac{P_1 - P_2}{\Delta r} dt \quad (3)$$

In this Euler equation, the pressure gradient was approximated by the ratio of pressure difference over spacing distance Eq. (4). It should be noted that this approximation stays valid at low frequencies (longer wavelengths), but will introduce errors at higher frequencies (short wavelengths).

$$\frac{\partial P}{\partial r} = \frac{\Delta P}{\Delta r} \quad (4)$$

The instantaneous intensity field is then determined as the average product of the pressure field and the particle velocity field.

$$I_r \left[W/m^2 \right] = \overline{p(t) \cdot v_r(t)} \quad (5)$$

The intensity can be calculated in real-time by the following formula using a time averaging process:

$$I = -\frac{P_1 + P_2}{2\rho\Delta r} \int (p_1 - p_2) dt \quad (6)$$

In the Brüel & Kjær PULSE multi-analyzer system, intensity is calculated as an "active intensity spectrum," meaning that the sound field calculated is actually the one that contributes to the net flow of energy.

The sound intensity component I is calculated from the complex one-sided cross-spectrum between the two microphones, the spacing between the microphones and the air density. This is calculated as:

$$I_r(\omega) = -\frac{1}{\omega\rho\Delta r} \Im \{ G_{xy}(\omega) \} \quad (7)$$

where ω is the angular frequency, ρ is the density of the acoustic media and G_{xy} is the cross-spectrum between the 2 microphone signals. Figure 2 shows a typical averaged sound intensity spectrum where the two colors show the intensity contributions in the positive and negative direction (1/3 octave

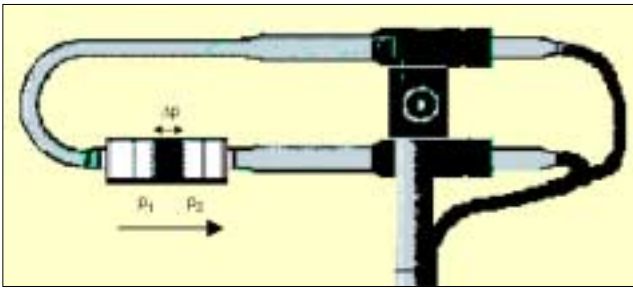


Figure 1. Sound intensity probe.

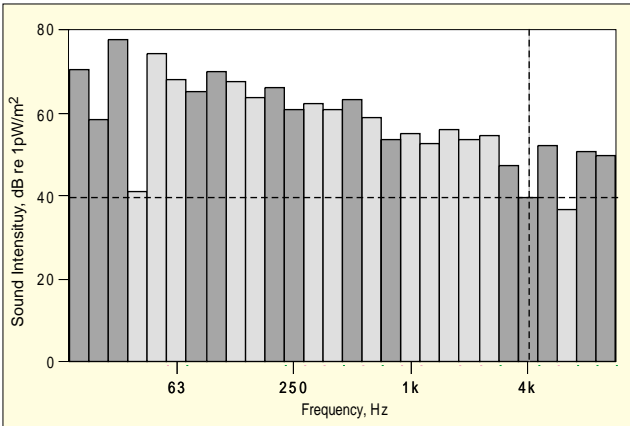


Figure 2. 1/3 octave sound intensity spectrum.

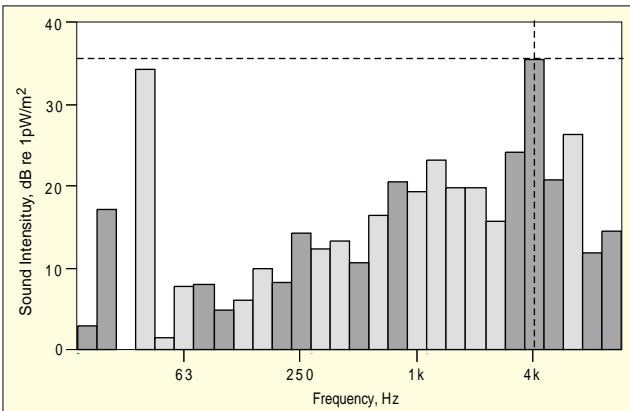


Figure 3. P-I index spectrum.

bands).

It is also important to evaluate the difference between the sound intensity level and the sound pressure level. The descriptor measured in that case is called the P-I index. The P-I index is equivalent to the mean pressure level minus the sound intensity level. The P-I descriptor will determine the low frequency limit of the measurement. Figure 3 shows an example of a P-I index spectrum measured in 1/3 octave bands.

In sound intensity mapping, the sound intensity spectra are measured at different discrete points of a grid, then displayed on a contour plot (Figure 4). The sound intensity vectorial distribution can then be displayed for a certain frequency range and one can superimpose the contour spectral results on top of a picture of the tested object allowing for a precise location and documentation of noise sources. An example is shown in Figure 5.

Benefits:

- Because sound intensity is a vector quantity, the acoustic field can be represented as amplitude and direction.
- True measure of acoustic radiation by determination of energy flow.
- Possible determination of sound power from sound intensity measurements.
- Measurements in-situ (relatively tolerant to background and



Figure 4. Sound intensity measurement procedure on a car engine.

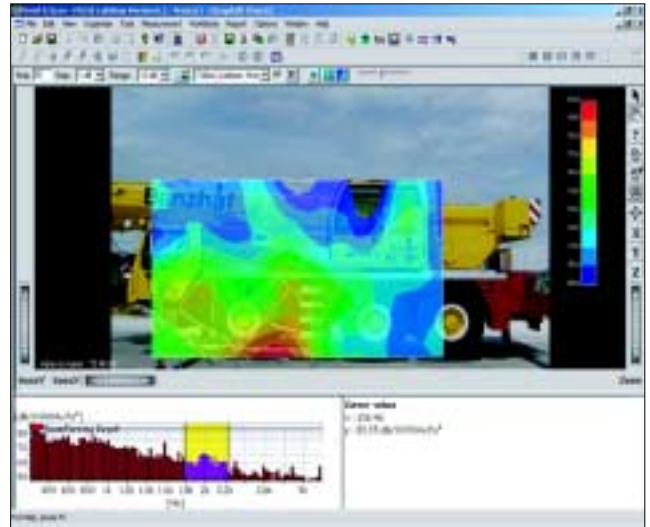


Figure 5. Sound intensity contour map produced by a PULSE system.

uncorrelated noise).

- Portable technique (can be used with a two channel sound level meter).

Limitations:

- Frequency limitations due to the pressure approximation gradient (determined by the microphone spacing); up to 10 kHz with the smallest spacing.
- Relatively time-consuming.
- Accurate equipment required (accurately phase-matched microphones, and data acquisition system).
- Sources need to be stationary.

Selective Intensity. Intensity measurement and mapping are effective ways to determine the location, absolute power and relative contribution of individual sub-sources as observed on the surface of an object ('hot-spots'). However, when it comes to identifying the internal root causes for the radiated noise, this method only gives indirect indications (e.g., the spectral content of the noise). Selective intensity provides a direct way to measure whether an external 'hot-spot' is related to a specific internal root cause.

The principle of selective intensity technique is to calculate the part of the intensity that correlates with a reference signal (accelerometer, microphone or any other transducer placed in the location of a suspected main cause of sound radiation) as shown in Figure 6. The selective intensity spectrum will be close to the full intensity spectrum if the suspected radiation location is correct. An example is shown in Figure 7.

Benefits Compared to Traditional Sound Intensity:

- Determination of sound intensity coherent to a reference signal.
- More precise localization of source radiation.
- Can be measured simultaneously with traditional sound intensity.



Figure 6. Selective Intensity principle.

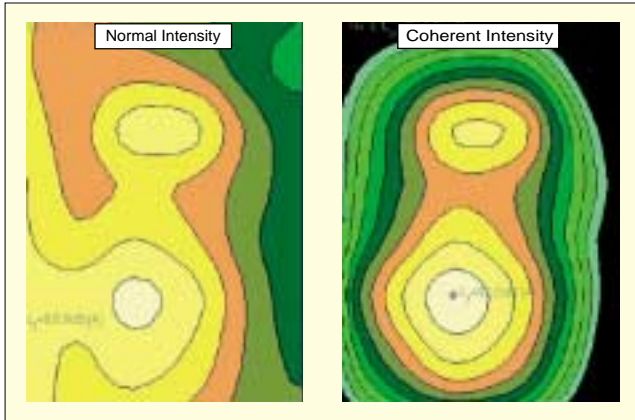


Figure 7. Comparison of sound intensity mapping of a loudspeaker with and without coherence.

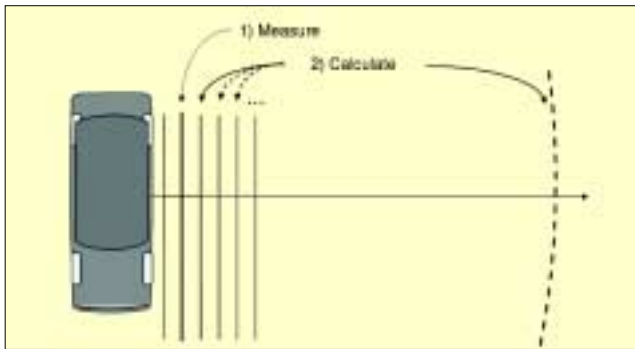


Figure 8. STSF principle.

Spatial Transformation of Sound Fields (STSF)

Overview. The basic principle of STSF is illustrated in Figure 8. Based on measured cross-spectra in a reference scan plane, this technique determines all acoustical parameters in extended regions. The sound fields can be calculated using Near-field Acoustic Holography (NAH) techniques or Helmholtz integral equation techniques which involve deriving solutions of the homogeneous wave equation in the far-field.³⁻⁶

This technique is similar to the holograms in optics where the magnitude and phase of a coherent light is recorded on film. In acoustic holography, the magnitude and phase (relative to references) of the sound field are measured from a level map (flat image) of the sound pressure level in the measurement plane.

In this technique, an array of microphones is used to scan a particular region, with reference transducers in fixed locations, as shown in Figure 9.

The STSF key words are:

- Near-field calculations – pressure distribution, intensity mapping, vector intensity.
- Far-field calculations – directivity patterns, SPL along a line, contribution analysis.
- Source attenuation and possible solutions – simulations, “what if” scenarios.



Figure 9. STSF measurement example on a tire.

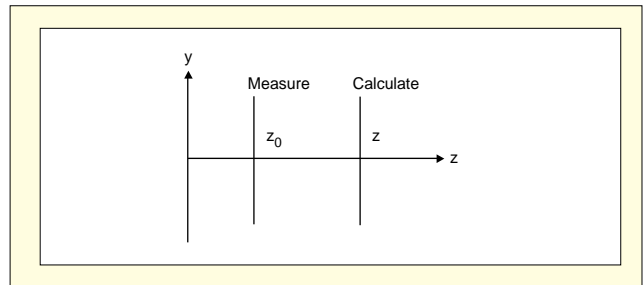


Figure 10. Holography coordinate convention.

NAH Theoretical Background. Near-field Acoustic Holography allows the study of spatial and frequency (or time) dependence of acoustic fields. Rather than measuring all points in 3D space directly, NAH is used to reconstruct the quantities of an acoustic field above and below the measured hologram plane, allowing for the data-acquisition process to be considerably shortened.

The theory of NAH is based on the Helmholtz integral equation and the two-dimensional spatial Fourier transform. Complex pressure on a plane parallel to the hologram plane is computed by the inverse 2D FFT of the product of hologram pressure spectra and modified Green's functions. The acoustic velocity vector is then acquired using Euler's equation, where the active and reactive intensity vectors are the real and imaginary parts of the product of computed complex pressure and conjugate acoustic velocity.

The 3D wave equation is expressed as follows using the following convention for the axis:

$$\nabla^2 p - \frac{1}{c^2} \frac{\partial^2 p}{\partial t^2} = 0 \quad (8)$$

$\nabla^2 = \nabla \cdot \nabla$ is the Laplace operator (Nabla squared operator), which will compute the scalar divergence of the complex sound pressure (partial derivatives with respect to spatial coordinates x, y, z). r is the position in space and c is the speed of sound. It is also possible to represent this wave equation in the frequency domain, by assuming sinusoidal wave components and introducing a wavenumber k :

$$\nabla^2 p + k^2 p = 0 \quad (9)$$

with

$$k = \frac{\omega}{c} \quad (10)$$

The Helmholtz Integral Equation (HIE) can then be derived from the wave equation, and the wave field can be expressed at a position outside a closed surface that encloses the source. The most general form of this Kirchhoff-Helmholtz integral is expressed as:

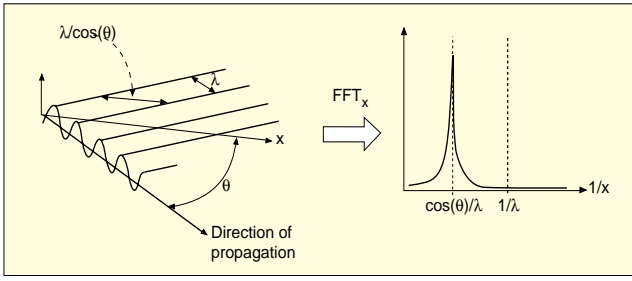


Figure 11. Spatial Fourier transform of sound field.

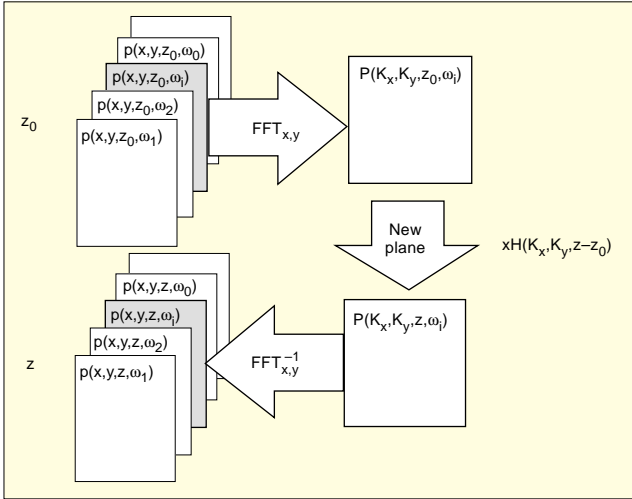


Figure 12. Holography computation principle.

$$p(\vec{r}) = -\frac{1}{4\pi} \iint_S [G(\vec{r}|\vec{r}_0) \nabla p(\vec{r}_0) - p(\vec{r}_0) \nabla G(\vec{r}|\vec{r}_0)] \cdot \vec{n} dS \quad (11)$$

where G is Green's function defined as:

$$G(\vec{r}|\vec{r}_0) = \frac{e^{-jk|\vec{r}-\vec{r}_0|}}{4\pi|\vec{r}-\vec{r}_0|} \quad (12)$$

Introducing the spatial Fourier pair:

$$\begin{cases} \tilde{P}(k_x, k_y, z, \omega) = \int_{-\infty}^{\infty} \int_{-\infty}^{\infty} p(x, y, z, \omega) e^{j(k_x x + k_y y)} dx dy \\ p(x, y, z, \omega) = \frac{1}{4\pi^2} \int_{-\infty}^{\infty} \int_{-\infty}^{\infty} \tilde{P}(k_x, k_y, z, \omega) e^{-j(k_x x + k_y y)} dk_x dk_y \end{cases} \quad (13)$$

All these formulations use the conventional coordinate system represented in Figure 10.

The equation can be written in the form:

$$p(x, y, z - z_0, t) = h(x, y, z - z_0, t) * p(x, y, z_0, t) \quad (14)$$

↓
Spatial 2D-Fourier Transform
↓

$$\tilde{P}(k_x, k_y, z, t) = \tilde{H}(k_x, k_y, z - z_0, t) \cdot \tilde{P}(k_x, k_y, z_0, t)$$

with the expression of the Transfer function:

$$\tilde{H}(k_x, k_y, z - z_0) = e^{-jk_z(z - z_0)} \quad (15)$$

Figure 11 explains how spatial frequencies are related to the direction of propagation and wavelength, using the spatial Fourier decomposition.

The FFT process is shown in Figure 12 where the new plane is calculated using the HIE. It illustrates a block-diagram of the calculation process in STSF, where the pressure further away from the source is calculated using a 2-dimensional propagation kernel. Each plane is calculated at each individual frequency and the sampling interval must be high enough to avoid spatial aliasing in the calculations.

The k_z wave number is expressed in terms of the 3 other wave numbers as follows:

$$k_z^2 = k^2 - k_x^2 - k_y^2 \quad (16)$$

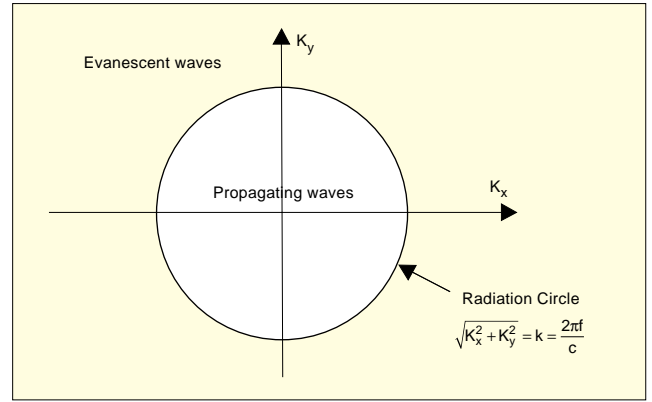


Figure 13. Radiation circle representation.

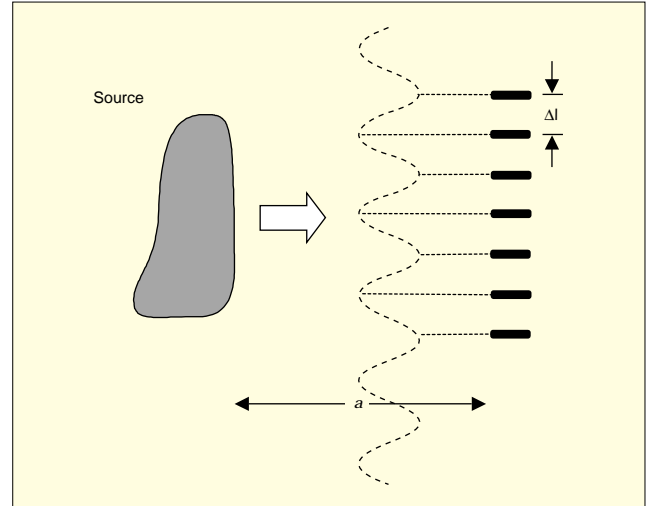


Figure 14. Grid spacing for STSF measurement.

Two cases can occur depending on the value of this wave number k_z :

1. Propagating Plane waves case:

$$k_z = \sqrt{k^2 - k_x^2 - k_y^2} \text{ for } k_x^2 + k_y^2 \leq k^2 \quad (17)$$

2. Evanescent waves case (vanishing waves):

$$k_z = -j\sqrt{k_x^2 + k_y^2 - k^2} \text{ for } k_x^2 + k_y^2 > k^2 \quad (18)$$

Depending on the value of the wavenumber k_z , plane waves are propagating or exponentially decaying (evanescent case). The evanescent wave will propagate in the (x,y) plane but will decay exponentially in the z direction (direction of propagation). This decay will increase with higher values of spatial frequencies.

A geometrical representation can be made depending on the propagating or evanescent case. The boundary between the evanescent and propagating case is called the radiation circle (Figure 13).

Measurement Techniques. In theory, an STSF measurement could be performed using a minimum of instrumentation consisting of a reference transducer, a scan microphone, a cross-spectrum analyzer and a computer. Due to the quantity of data involved, such a measurement would be unacceptably slow. A practical system includes a set of reference transducers, an array of scan microphones, an automated positioning system (i.e., a robot), a multi-channel data acquisition system and a computer. Due to the 2-dimensional spatial FFT process, the measurement points have to form a regular rectangular grid.

The resolution criterion is shown in Figure 14. If λ_{\min} is the wavelength of the highest frequency wave in the analysis and to avoid any spatial aliasing, the spacing between microphones should be

$$\Delta l \leq \frac{\lambda_{\min}}{2} \text{ and } \Delta l \leq a \quad (19)$$

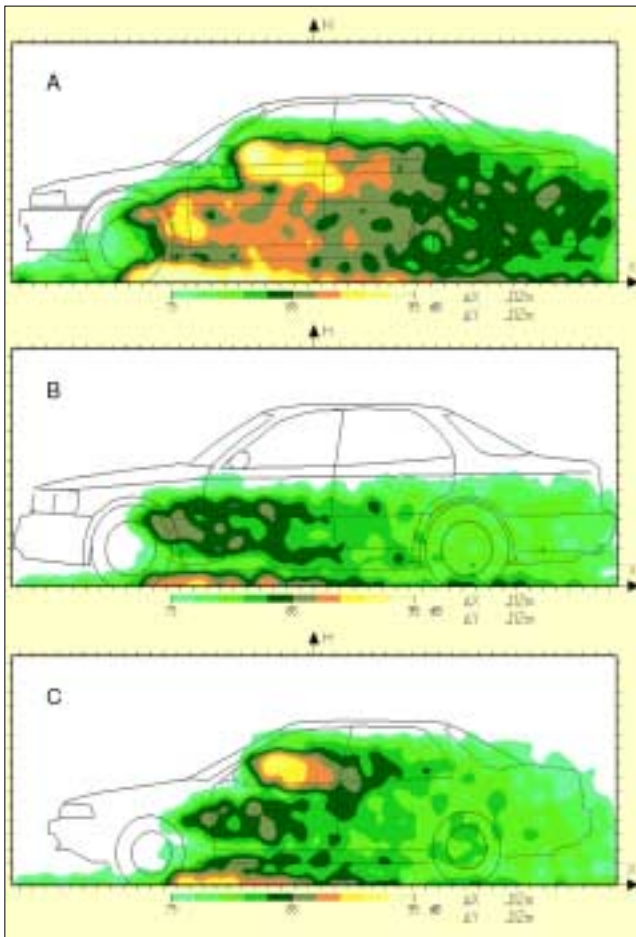


Figure 15. Wind tunnel results on 3 different car models.

where a is the distance between the radiation source and the array of microphones.

An important assumption about the STSF technique is that all auto and cross spectrum calculations are repeatable. This assumption is valid if the sound source is stationary, and a sufficient bandwidth, block time product (BT product) is available for the analysis.

Applications. In this first example, three cars in a wind tunnel were measured. A reference microphone was used in the cabin of the car near the driver's head. This ensures that only the sound radiation from the airflow coherent with the reference microphone will be determined. Noise caused by turbulent flow of air across the diaphragms of the array microphones will be neglected.

Each car was exposed to airflow at about 100 km/h. As seen in Figure 15, Car A shows the highest levels of aerodynamic noise, generated at the exterior mirror and front wheel. The results also show that Car B is the quietest car, radiating the least noise to the driver's ear.

In the following example, airborne noise transmission was investigated in a car. A white noise sound source was placed inside the cabin. An array of microphones scanned the area of interest in a semi-anechoic environment.

Active intensity measurement results (from 250 to 3250 Hz) showed that noise was radiated at the joints of the front and rear doors with an extremely high resolution. STSF is an excellent investigation tool for leaks.

Benefits:

- Ease of use.
- Fast and very reliable.
- Excellent resolution (very good separation of closely located uncorrelated sources).
- Provides a complete 3D description of both the near-field and far-field (particle velocity, intensity vectors, partial sound power, noise source ranking and sound pressure).

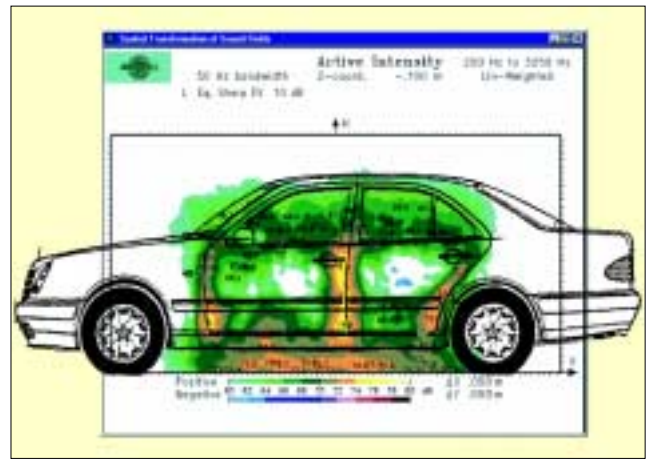


Figure 16. Airborne transmission noise on a car.



Figure 17. NS-STSF technique, full-sized microphone array.

- Can be used in tougher environmental conditions.
- Possible suppression of uncorrelated background noise thanks to a precise cross-spectral measurement principle.
- Provides calibrated maps of sound intensity, pressure and particle velocity close to the source.

Limitations:

- Limited frequency range (depending on the spacing of the measurement points in the grid), typically valid up to 6.4 kHz.
- Can only be used with stationary sound fields.

Non-Stationary STSF

Non-stationary STSF is a time domain based acoustic holography technique. This technique is a unique application that takes into account noise source locations that radiate nonstationary acoustic waves. The Time Domain Holography technique characterizes all sound field descriptors (pressure, particle velocity, intensity, etc.) as a function of time or RPM. Using this technique, a lot of mechanical problems can be tackled involving transient sounds, squeaks, or other nonstationary, order related components.⁷

NS-STSF outputs a time sequence of snapshots of a selected acoustical parameter in a calculation plane parallel to the measurement plane, combining time and space resolution principles. The time resolution is indeed very high, since this technique involves a separation of acoustic snapshots being equal to the sampling interval of the A/D converter of the data acquisition system.

In this technique, the measurement is performed using a fixed

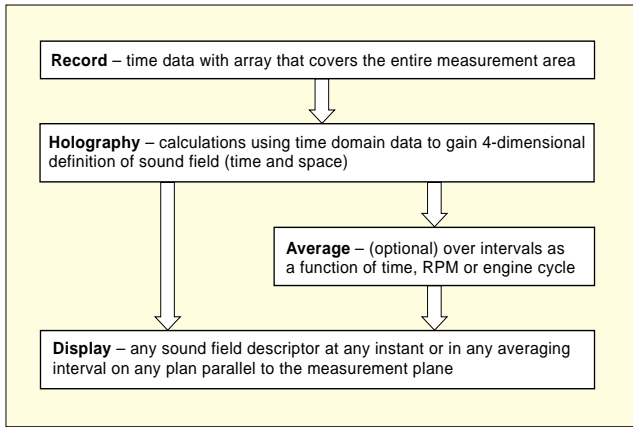


Figure 18. NS-STSF analysis flow.

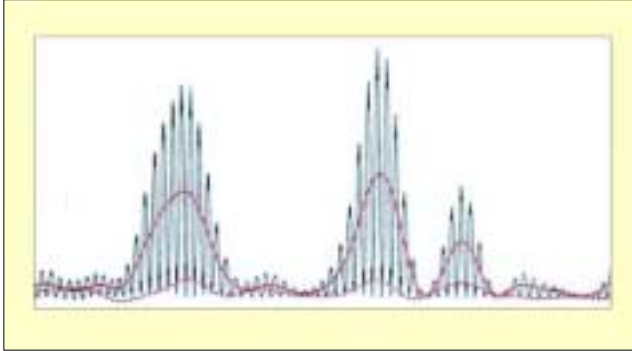


Figure 19. Instantaneous intensity: active component (red solid), reactive component (red dashed).

array of microphones, and all signals are measured simultaneously. The data flow in a NS-STSF procedure is represented in Figure 18, from recording to displaying the results.

Theory background. Using the same convention as Figure 10 for the coordinates, it is possible to introduce the spatial and temporal Fourier transform pairs:

$$\begin{cases} \tilde{P}(k_x, k_y, z, \omega) = FFT_t \left[\int_{-\infty}^{+\infty} \int_{-\infty}^{+\infty} p(x, y, z, t) e^{j(k_x x + k_y y)} dx dy \right] \\ p(x, y, z, t) = FFT_t^{-1} \left[\int_{-\infty}^{+\infty} \int_{-\infty}^{+\infty} \tilde{P}(k_x, k_y, z, \omega) e^{-j(k_x x + k_y y)} dk_x dk_y \right] \end{cases} \quad (20)$$

Introducing those Fourier transform pairs in the wave equation, we obtain the following expression:

$$\left[\frac{\partial^2}{\partial z^2} + k_z^2 \right] \tilde{P}(k_x, k_y, z, \omega) = 0 \quad (21)$$

with

$$k_z^2 = k^2 - k_x^2 - k_y^2 \quad (22)$$

A complete solution to Equation 21 can be written as follows using an inverse Fourier transform process:

$$\begin{aligned} \tilde{P}(k_x, k_y, z, \omega) &= \tilde{P}(k_x, k_y, z_0, \omega) e^{-jk_z(z-z_0)} \\ &\downarrow \\ &\boxed{FFT^{-1}} \\ &\downarrow \\ p(x, y, z, t) &= \frac{1}{(2\pi)^3} \int_{-\infty}^{+\infty} \int_{-\infty}^{+\infty} \tilde{P}(k_x, k_y, z, \omega) e^{-j(k_x x + k_y y)} dk_x dk_y \end{aligned} \quad (23)$$

Waves situated outside the radiation circle will be evanescent, decaying exponentially in amplitude in the z direction (away from the source), while waves situated inside the circle will propagate.

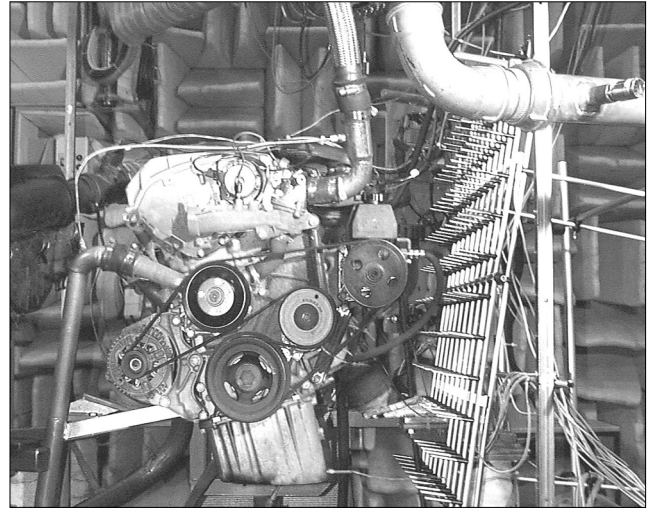


Figure 20. Non-stationary holography set-up on an engine.

Using the well-known mass-conservation rule for nonviscous fluids,

$$\rho \frac{\partial \bar{u}}{\partial t} = -\nabla p \quad (24)$$

the particle velocity can be then expressed as:

$$\bar{u}(x, y, z, t) = \frac{1}{\rho c (2\pi)^3} \int_{-\infty}^{+\infty} \int_{-\infty}^{+\infty} \int_{-\infty}^{+\infty} \tilde{P}(k_x, k_y, z, \omega) \frac{\bar{k}}{k} e^{-j(k_x x + k_y y - \omega t)} dk_x dk_y d\omega \quad (25)$$

where $\bar{k} \equiv \{k_x, k_y, k_z\}^T$ is the normalized wave number vector and ρc is the impedance of air.

The instantaneous intensity vector can then be calculated using the product of expressions for the pressure field and the particle velocity. This instantaneous acoustic intensity will consist of an envelope active and reactive part. The reactive part describes spatially oscillating energy that does not carry any energy flow. The active part is the oscillating portion of the intensity around a time varying local average peak value near the active component. The envelope active and reactive components are then calculated using Hilbert transforms of the pressure and particle velocity expressed above.

The corresponding analytic signals are then expressed as:

$$p_c(\bar{r}, t) = p(\bar{r}, t) + j\tilde{p}(\bar{r}, t) \quad (26)$$

$$\bar{u}_c(\bar{r}, t) = \bar{u}(\bar{r}, t) + j\tilde{\bar{u}}(\bar{r}, t) \quad (27)$$

The complex intensity is then determined by the product of those two signals, leading to the expressions of the active and reactive components of the intensity (real and imaginary parts):

$$\bar{I}_c(\bar{r}, t) = \frac{1}{2} \langle p_c(\bar{r}, t) \cdot \bar{u}_c^*(\bar{r}, t) \rangle \quad (28)$$

$$\begin{cases} \bar{I}_{\text{active}}(\bar{r}, t) = \frac{1}{2} [p(\bar{r}, t) \cdot \bar{u}(\bar{r}, t) + \tilde{p}(\bar{r}, t) \cdot \tilde{\bar{u}}(\bar{r}, t)] \\ \bar{I}_{\text{reactive}} = \frac{1}{2} [\tilde{p}(\bar{r}, t) \cdot \bar{u}(\bar{r}, t) - p(\bar{r}, t) \cdot \tilde{\bar{u}}(\bar{r}, t)] \end{cases} \quad (29)$$

Applications. A sufficiently large array (>90 channels) is typically used in NS-STSF. Figure 20 shows a picture of a measurement setup taken on the front and side of an engine.

The NS-STSF technique is capable of performing averaging into a set of angle intervals of specified width. Figure 21 shows the active intensity in the 1 kHz 1/3 octave band averaged over a 10° interval. Both contour plots represent a crank angle interval centered at 50° but show two different crank angle slices. To the left, the angle slice shows that this is the position where the intensity radiated from the oil sump in the engine is maximum. The right slice of the figure shows a contour cursor above the fan belt roller of the engine, still at the same crank angle interval.

Figure 22 shows the same crank angle comparison but in this

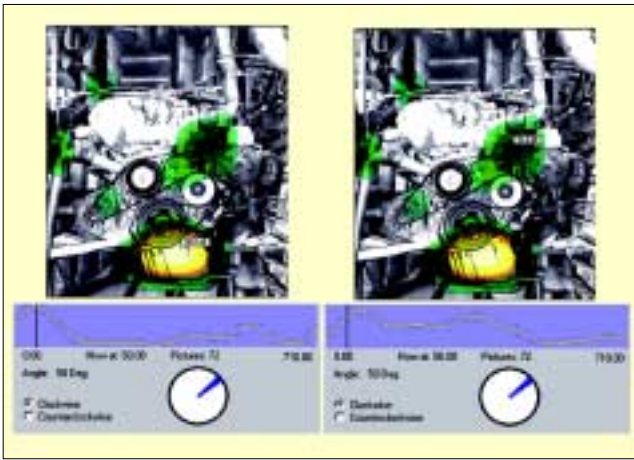


Figure 21. 1 kHz active intensity averaged over a 10° crank angle interval, 50° after the firing of the front cylinder.

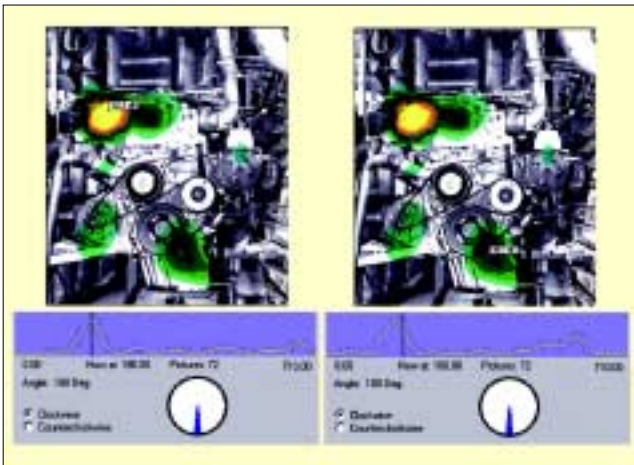


Figure 22. 1 kHz active intensity averaged over a 10° crank angle interval 180° after the firing of the front cylinder (half-angle rotation after firing of the front cylinder).

case the contour cursor is placed over the valve cover. The radiation investigated corresponds to an angle that is maximum at the valve cover. Here, the crank angle is at 180° (half-angle rotation). This example shows how the impulsive radiation from the oil sump precedes the impulsive radiation from the valve cover, as the angle slice for the radiation from the oil sump exhibits a peak before the peak radiation of the valve cover.

Similar run-up type measurements can be performed using NS-STSF. Time-frequency representations are always useful in those configurations, where different harmonic or sub-harmonic components can be detected and followed with RPM changes or fluctuations.

Figure 23 shows the time-frequency representation (Short Time Fourier Transform) of the measured sound pressure level at the oil pump (single microphone). A time slice at 1072 Hz and a frequency spectrum at 9.04 sec are selected from the contour display.

Figure 24 shows the intensity maps at 4950 RPM for the front and the left of the engine. The dominating radiation appears between the power steering pump and the air intake manifold.

Benefits:

- Very fast single shot technique.
- Easy to use.
- Excellent spatial and temporal resolution.
- All time domain averaging techniques are possible (time synchronous averaging, crank angle averaging, order tracking averaging, transient analysis); will show both *where* and *when* noise is radiated.
- Projection of sound fields both in near- and far-fields.
- Sound source ranking allows for filtering before the averaging process.

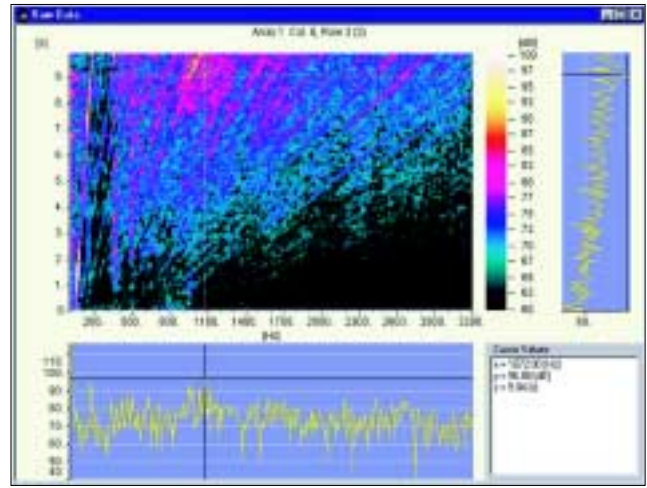


Figure 23. Time frequency plot of engine run-up microphone signal placed near the oil sump.

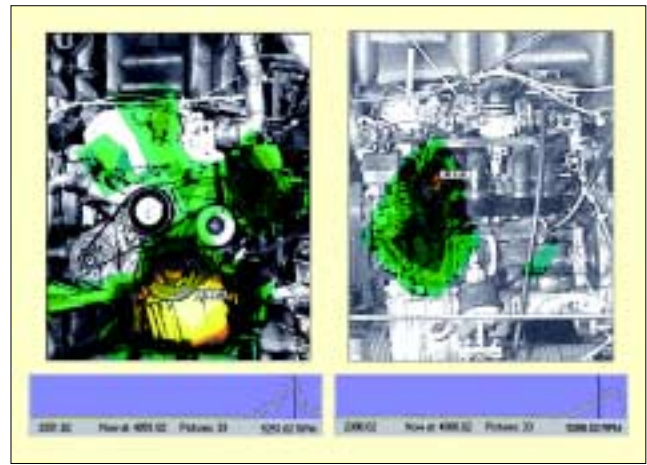


Figure 24. Calculated active intensity of 13th order at the front and left side of the engine (average value from 100 to 4950 RPM).

- Provides very comprehensive documentation for the complete sound field parameters.
- Limitations:**
- Requires a large number of microphones and measurement channels.
 - Requires free-field conditions.
 - Very intensive algorithms can lead to long calculation times.

Beamforming

Beamforming is a fairly recent technique for noise “root cause” investigations. It has been applied to the identification of airplane noise (wind-tunnel applications), trains in pass-by applications and is now being introduced to the automotive industry.

Beamforming is very similar to a ‘camera,’ in the sense that the array of microphones behaves as a lens. By varying the distance between the array and the object, sound fields can be determined for objects of many sizes with a wider frequency range and bandwidth. Beamforming is widely used in applications for exterior vehicle noise (outdoor, indoor) or wind-tunnel applications (exterior and interior). It provides a directional source map from the position of the array with a useful opening angle of 60°.

The beamforming technique is based on a delay-sum principle, where a planar array of microphones is used to capture the plane wave. The signals are then connected to a signal-processor to determine directional characteristics of the incoming sound.⁸

Theory background. As shown in Figure 26, a planar array of microphones is considered at locations r_m ($m=1, 2, \dots, M$).

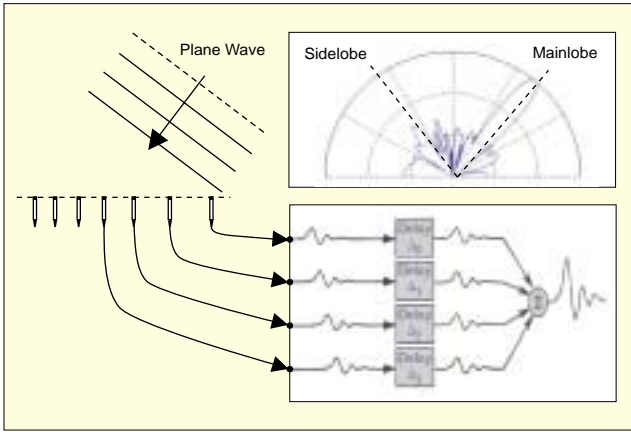


Figure 25. Individual Δ_m chosen such that signals (plane waves) arriving from a chosen direction will add up coherently.

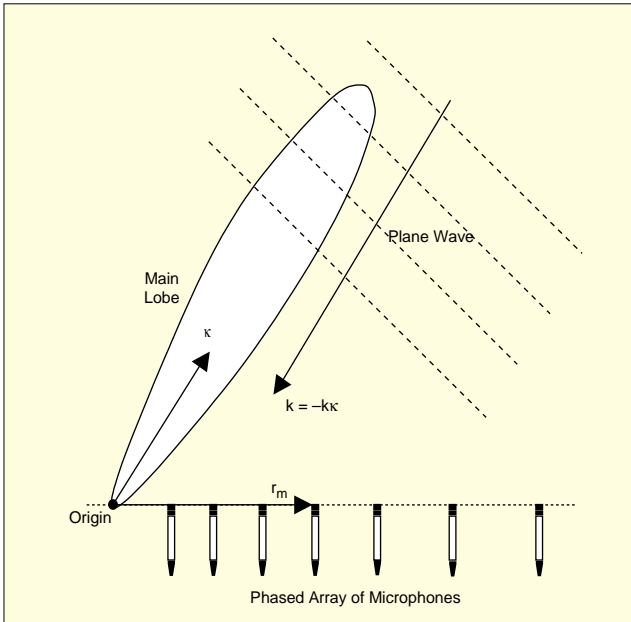


Figure 26. Illustration of a phased microphone array, a directional sensitivity represented by a mainlobe and a plane wave incident from the direction of the mainlobe.

When such an array is applied for Delay-and-Sum Beamforming, the measured pressure signals p_m are individually delayed and then summed as follows:

$$z(\vec{\kappa}, t) = \sum_{m=1}^M p_m(t - \Delta_m(\vec{\kappa})) \quad (30)$$

The individual time delays Δ_m are chosen with the aim of achieving selective directional sensitivity in a specific direction, characterized by a unit vector κ . This objective is met by adjusting the time delays in such a way that signals associated with a plane wave, incident from the direction κ , will be aligned in time before they are summed. Geometrical considerations show that this can be obtained by choosing:

$$\Delta_m = \frac{\vec{\kappa} \cdot \vec{r}_m}{c} \quad (31)$$

where c is the propagation speed of sound. Signals arriving from other far-field directions will not be aligned before the summation, and therefore will not coherently be added. The frequency domain version of Eq. (30) for the Delay-and-Sum Beamformer output is:

$$\tilde{Z}(\vec{\kappa}, \omega) = \sum_{m=1}^M P_m(\omega) \cdot e^{-j\omega\Delta_m(\vec{\kappa})} = \sum_{m=1}^M P_m(\omega) \cdot e^{j\vec{k} \cdot \vec{r}_m} \quad (32)$$

where $\mathbf{k} \equiv -k\kappa$ is the wave number vector of a plane wave incident from the direction κ in which the array is focused and $k =$

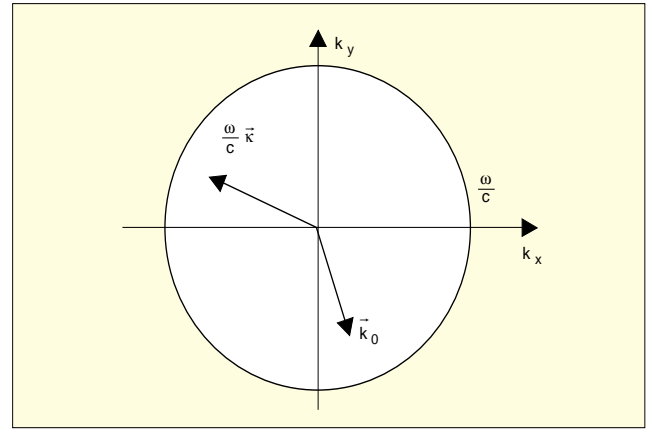


Figure 27. Projection of waves numbers on (k_x, k_y) plane.

ω/c is the wave number. Through the choice of time delays $\Delta_m(\kappa)$, or equivalently of the 'preferred' wave number vector $\mathbf{k} \equiv -k\kappa$, the beamformer was 'tuned' in the far-field direction κ . Ideally one would like to measure only signals arriving from that direction, in order to get a perfect localization of the sound source. To investigate how much 'leakage' will be generated from plane waves incident from other directions, we assume a plane wave incident with a wave number vector \mathbf{k}_0 different from the preferred $\mathbf{k} \equiv -k\kappa$. The pressure measured by the microphones will then be:

$$P_m(\omega) = P_0 e^{-j\vec{k}_0 \cdot \vec{r}_m} \quad (33)$$

which according to Eq. (32) will give the following output from the beamformer:

$$\tilde{Z}(\vec{\kappa}, \omega) = P_0 \sum_{m=1}^M e^{j(\vec{k} - \vec{k}_0) \cdot \vec{r}_m} \equiv P_0 W(\vec{k} - \vec{k}_0) \quad (34)$$

Here, the function W

$$W(\vec{k}) \equiv \sum_{m=1}^M e^{j\vec{k} \cdot \vec{r}_m} \quad (35)$$

is the so called Array Pattern, defined entirely by the array geometry. It has the form of a generalized spatial DFT (Digital Fourier Transform) of a weighting function, which equals 1 over the array area and 0 outside. Because the microphone positions \vec{r}_m have z-coordinate equal to 0, the Array Pattern is independent of K_z . We shall therefore consider the Array Pattern W only in the (k_x, k_y) plane, i.e., we consider the projections of the wave number vectors onto that plane (Figure 27).

There, W has an area with high values around the origin with a peak value equal to M at $(k_x, k_y) = (0, 0)$. According to Eq. (34), this peak represents the high sensitivity to plane waves coming from the direction κ , in which the array is focused. Figure 25 contains an illustration of that peak, called the mainlobe. Other directional peaks (sidelobes) will cause waves from such directions to leak into the measurement of the mainlobe direction κ . This will produce false peaks and images in a measured directional source map (also called ghost images). A good phased array design can therefore be characterized by having low Maximum Sidelobe Level (MSL) measured relative to the mainlobe level. With reference to Eq. (34), both \mathbf{k} and \mathbf{k}_0 have length equal to the wave number k , and they can have opposite direction, pointing for example in the positive and negative x-axis directions or such that $|\mathbf{k} - \mathbf{k}_0| \leq 2k$. Therefore, at a given frequency ω only the section $|\mathbf{K}| \leq 2k = 2\omega/c$ of the Array Pattern will be 'visible.' And if the Array Pattern has low MSL for $|\mathbf{K}| \leq K_{\max} = 2\omega_{\max}/c$ then a beamformer application will provide accurate directional source maps with a low degree of false images up to the frequency $\omega_{\max} = \frac{1}{2}K_{\max}c$. If the beamformer will be focused on directions κ not more than 30° off-axis, then the projection of the wave number vector $\mathbf{k}(\kappa) - \mathbf{k}_0$ on the array plane will be shorter than $(3/2)k$. Therefore only the section $|\mathbf{K}| \leq (3/2)k = (3/2)\omega/c$ will be visible, so the upper limiting frequency becomes $\omega_{\max}(30^\circ) = (2/3)K_{\max}c$.

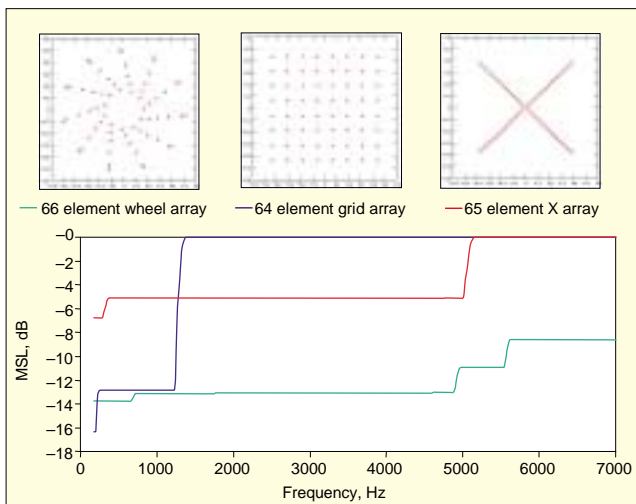


Figure 28. Comparison of 3 array designs.

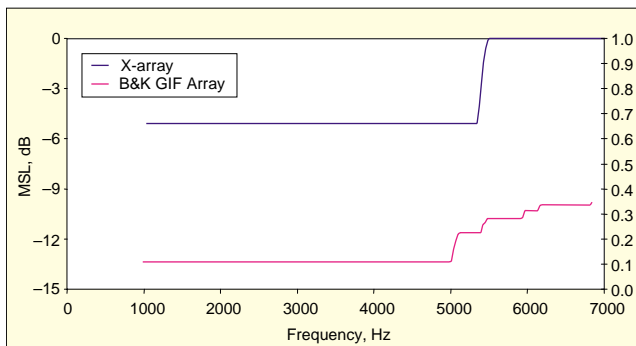


Figure 29. MSL comparison for X-array and B&K GIF design.

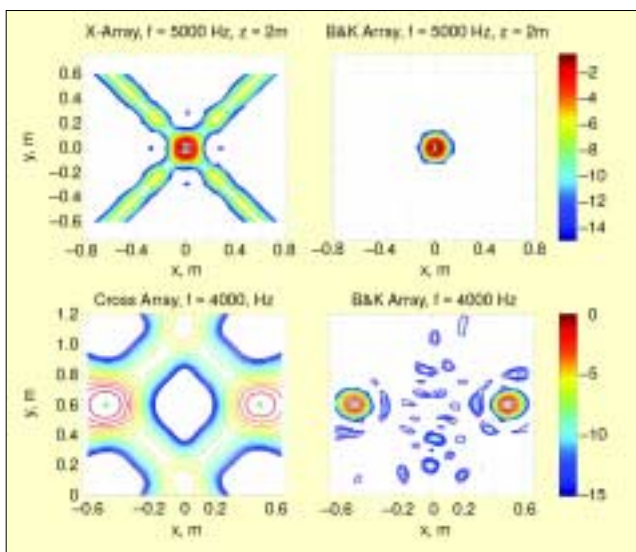


Figure 30. High-level sidelobe interference of the X-array compared to the GIF design.

The width of the mainlobe of the Array Pattern can be estimated from the similarity of Eq. (34) with a 2D DFT of a 'rectangular' type of spatial window function covering the area of the array. The mainlobe width will be inversely proportional to the diameter D of the array, and the first 'null' will be approximately at $|\mathbf{K}| = K_{\min} = 2\pi/D$.

Optimal Array Geometries. The beamformer performance is determined by its ability to suppress side lobes relative to the mainlobe (the ability of the system to 'focus'). The main challenge in a beamformer device design is then to produce arrays that have a minimum MSL in the frequency of interest and that do not create false images.

Three array designs are compared in Figure 28. It is clear that



Figure 31. Example of a 90-channel Brüel & Kjær wheel array for beamforming. The wheel array depicted has 15 identical spokes with integrated cabling each carrying 6 microphones. The wheel diameter is 2.43 m (patent pending).

the 66 element wheel array (~1 m in diameter) gives the lowest MSL values across the frequency range compared to regular array designs. Regular arrays will introduce severe spatial aliasing, due to spacing between microphones being larger than half the wavelength. This aliasing problem will appear as ghost images in measured directional sources, and will not provide a precise localization of noise radiations.

As an example, the X-array response is compared to the B&K GIF (Ghost Image Free) array, for a monopole point source radiating towards the center of the array. The GIF array was able to locate the source without creating ghost images. The same comparison was achieved with two uncorrelated complex sources with results shown in Figures 29 and 30. The effect of high level sidelobes is clearly seen for the X-array.

Figure 31 shows an example of the new-patented wheel array design, consisting of an odd number of small identical line arrays arranged as spokes in a wheel with identical angular spacing between the spokes. This array is totally modular, meaning that all spokes can be easily detached from their support allowing for a multitude of array configurations as well as easy transportation of the array in a standard flight case. The performance of this array has proven to be superior to regular grid or Archimedes spiral type arrays, achieving the lowest MSL.

Applications. To demonstrate the capability of the beamforming technique, Figure 32 shows the results obtained from a car in a wind tunnel test, with a wind speed of 80 mph. The test was performed with a 90-channel wheel array parallel with the side of the car at a distance of 3.3 m. Data were captured using the Brüel & Kjær Acoustic Test Consultant type 7761, running a 90 channel PULSE multi-analysis system. All data

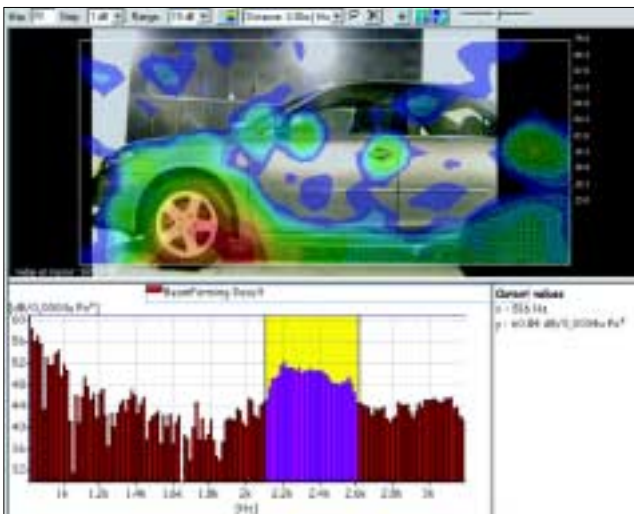


Figure 32. Beamforming result using the 90-channel B&K Wheel Array shown in Figure 31. The upper display shows the sound pressure levels resulting from the beamforming calculation as a contour plot. The lower display gives the spectrum at a point on door handle, and the highlighted interval (2.0-2.5 kHz) is the selected frequency range which the contour plot covers (screen-shot from the PULSE Beamforming application).

sets were then processed and displayed using the PULSE Beamforming application type 7768 for signal processing calculations.

Another application of beamforming is the measurement of an open car engine compartment. Figure 33 shows the measurement setup with a 66-element array, 1 m diameter array hanging 0.9 m above the engine. Figure 34 shows the result of a source map obtained for a frequency range of 6.3 kHz, with a resolution of about 5 cm. The engine was operating at 3500 RPM.

Benefits:

- Fast technique as all measurement channels are recorded simultaneously ('single-shot').
- Measurements on large objects (provides a 60° opening angle).
- High frequency range (> 20 kHz).
- Good resolution.
- Measurements are performed in the far-field (excellent for wind-tunnel applications).
- Possibility of pass-by or transient applications.

Limitations:

- Sound pressure maps are not calibrated (no calibration absolute levels near the source are obtained, as opposed to NAH/STSF techniques); only shows the relative contributions of the sound field at the array position.
- Requires a multi-channel data acquisition system, typically 60 channels or more.

Inverse Boundary Element Methods (IBEM)

The IBEM technique is often referred to as a general 3D holography method joining boundary element modeling with inverse methods. While traditional holography techniques provide planar measurements and calculations, IBEM allows degrees of freedom models and a representation of sound fields on a mapped geometry.

Boundary Element Methods. The boundary element method (BEM) is a widely used numerical technique for solving general radiation problems within acoustics, mainly at low to medium frequencies. Usually a forward problem is considered where the surface velocity of a structure is known and the radiated sound field is sought. Different techniques exist based on one of two formulations: direct or indirect.⁹⁻¹³

Direct techniques are the most common, as they are based on the Helmholtz integral equation and lead to a simpler implementation. This technique will formulate the problem in terms of pressure and normal velocity over the source surface.



Figure 33. Beamformer placed above an engine.



Figure 34. Beamforming source map at 6300 Hz for a car engine operated at 3500 RPM.

Indirect techniques are based on layer potentials. In this formulation, the exterior acoustic field is represented in terms of single and/or double-layered potentials. For example, a single layer formulation can be simply expressed in terms of the unknown source strength and a Green's function. These formulations can deal with more general problems, although the implementation is more difficult compared to the direct method.

The first step of a BEM investigation is the creation of a geometry and a surface discretisation of the geometry using boundary elements. The choice of the type of elements, their sizes and their density will be crucial and will determine the calculation time, as well as the relevancy of the results based on the wavelength of the sound fields.

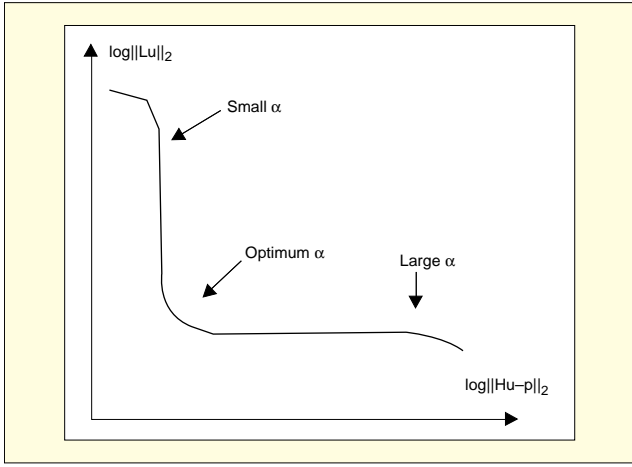


Figure 35. L-curve regularization.

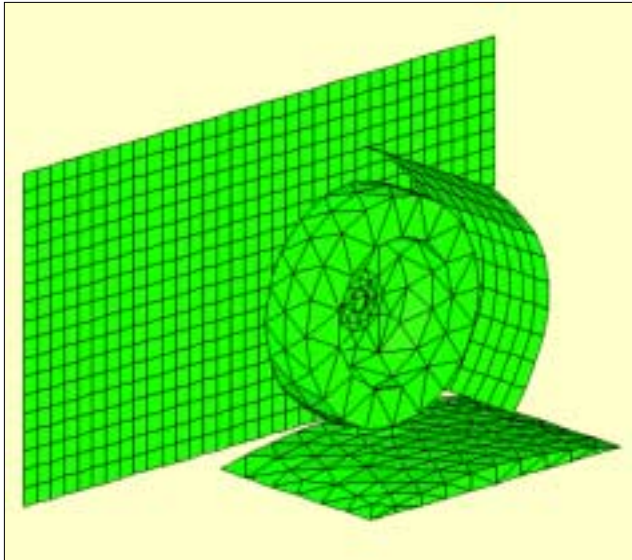


Figure 36. Plane and curved array mesh relative to boundary element mesh of tire/rim for standing tire.

Inverse Boundary Element Methods. Based on a BEM modeling of the exterior domain wrapping the sound source, it is possible to introduce an inverse problem. In this case, data are collected in the near-field rather than on the surface. The main goal is then to calculate boundary representations from field measurements in order to reconstruct the surface velocity distribution over the source surface. The inverse problem becomes much more difficult to solve than the forward problem mainly because of the intrinsic ill-posed nature of the problem.

In order to tackle this, sophisticated techniques now involve the SVD (Singular Value Decomposition) of a complex transfer function matrix \mathbf{H} , relating the pressure p at the microphone positions and the unknown node velocities \mathbf{v}_n (normal component).

$$\mathbf{p} = \mathbf{H}\mathbf{v}_n \quad (36)$$

\mathbf{v}_n being a vector that contains all unknown normal velocity components. The discrete inverse problem consists of determining the unknown values \mathbf{v}_n that produce the measured values in \mathbf{p} .

The matrix \mathbf{H} is always ill-conditioned because it still contains evanescent wave terms (decaying amplitude from the source surface). To completely tackle this problem, a regularization (= stabilization) technique is used on the transfer function matrix and added to the SVD process. The SVD formulation will tackle the common problem of ill-conditioning associated with Eq. (36).

The Tikhonov regularization is one of the most popular, efficient methods to make an ill-posed problem less sensitive to

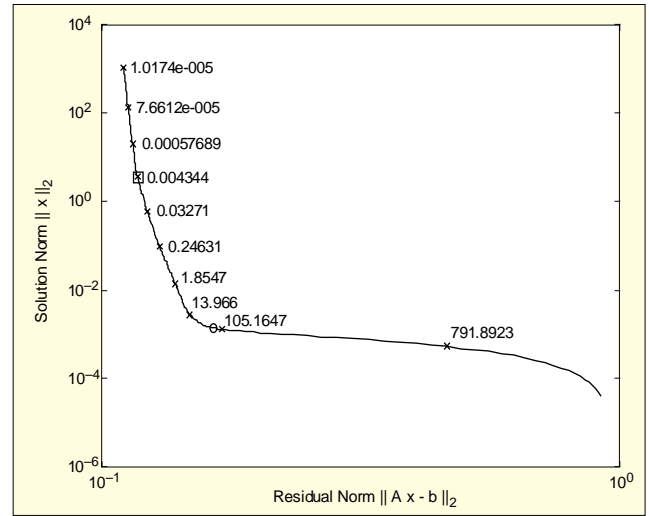


Figure 37. L-curve for Tikhonov regularization computed for the first principle component at 100 Hz. The optimum regularization parameters computed by the L-curve criterion (circle) and GCV method (square) are marked.

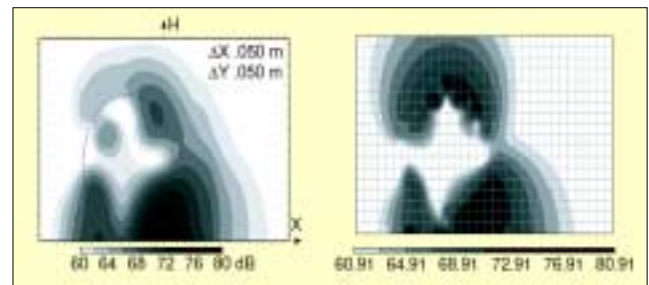


Figure 38. Sound pressure distribution on calculation plane by STSF and inverse BEM (L-curve) at 100 Hz.

errors in the measurement data. It is an efficient numerical technique for inverse problems where it is mainly used. Tikhonov regularized formulations solve a minimization problem expressed in terms of specific norms and semi-norms. In the case of this problem, they are used to smooth out the solutions while still fitting to the measurement data.

Choosing the amount of regularization is crucial in determining a stable and relevant solution of the formulated problem. In essence, this means determining whether a given SVD component contains useful information or is contaminated by error. For that purpose, a selection tool that automatically detects useful components is preferred. An L-shaped criterion is preferred over the classical GCV (Generalized Cross-Validation) approach because it provides a more robust reconstruction.

The L-curve gives a method for computing and locating an optimal regularization parameter, corresponding to the L-curve's corner. This parameter yields a smoother solution, as the discrete smoothing norm of the regularized solution is plotted versus the residual norm on a log-log scale (norms considered are L_2 Euclidian norms), as shown in Figure 35.

The L-curve plot will seek a balance between the perturbation error component and the regularization error component, α being the regularization parameter in the following formulation of the minimization problem:

$$\min_{u_n} \left[\|Hu_n - p\|_2^2 + \alpha^2 \|Lu_n\|_2^2 \right] \quad (37)$$

where \mathbf{L} is a regularization matrix reflecting an area weighting of the node velocities. The optimum value of the regularization parameter will then be found on the corner of the L-curve, at the best balance between "fit to data" and "small smoothing norm" (Figure 35).

Practical Examples

Tire measurements. A real tire structure excited by a vibra-

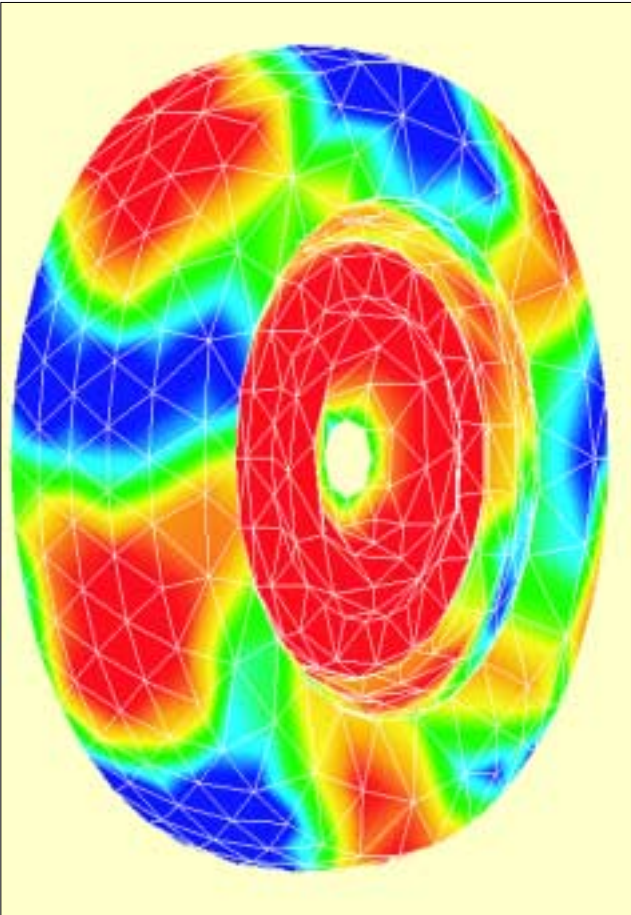


Figure 39. IBEM results of tire/rim model – average surface sound intensity at 60 Hz.

tion exciter is considered in this example. Measurements were taken using a linear array for a tire side measurement and a circular (curved) array for close measurements at the rear of the tire. Moreover, four reference microphones were distributed around the tire in order to derive a principal component description of the sound field. Two of these four reference microphones were placed on the ground in front of and behind the tire while the last two microphones were located in the air above the tire. A total of 821 measurement positions were used for this setup (Figure 36), the number of boundary nodes on the tire surface being 266.

Choosing the parameter α in a Tikhonov regularization is not a straightforward task, although several methods exist that do not require information about the norm of the error-vector contaminating the field pressure vector. Here we consider two methods for extracting an optimum regularization parameter. The first method which is very popular uses a GCV.¹⁴ The other approach is the so-called L-curve criterion, which is a plot of the smoothing norm vs. the residual norm. The resulting curve will often have a horizontal and a vertical part, and in between these parts we find solutions representing a balance between “fit to data” and “small smoothing norm.” Figure 37 shows the L-curve computed for the first principal component at 100 Hz. Note that the GCV method computes a parameter that can often be too small, typically the case if the error/noise component of the measured field pressure vector is not predominantly white.

In order to assess the reconstructed surface velocity on the tire structure, one can compute the sound field on a plane surface close to the tire-side. By doing so, a comparison of reconstructions obtained by inverse BEM with results obtained from Near-field Acoustical Holography (STSF) can be done. The total field is obtained by adding the principal fields resulting from the principal component description of the sound field. For the reconstructed sound pressure, Figure 38 shows

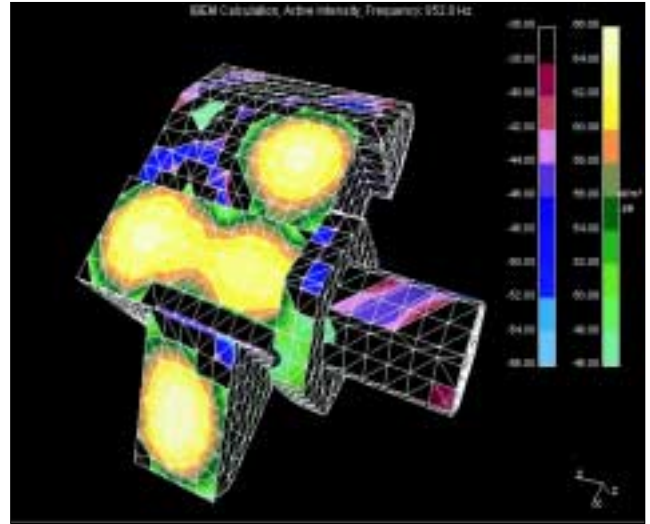


Figure 40. IBEM intensity results on a “wooden engine box” design, with 6 noise-simulator loudspeakers (Courtesy of Daimler Chrysler).

that the inverse BEM provides a sound field picture that is more or less identical to the plot from an STSF technique. The L-curve criterion applied to each principal component gives rise to meaningful reconstructed sound fields (although one cannot directly compare STSF and inverse BEM, as different filtering techniques are inherent in each individual method). The result that could be obtained from the GCV method is not shown here as it does not provide any meaningful information.

Figure 39 shows a complete surface velocity description of the tire and the surface sound intensity calculation distribution at a particular frequency. An excellent determination of the acoustic solution is then possible, as the software will determine for the user an optimum choice of regularization parameters.

Engine model. Figure 40 shows an example of a sound source reconstruction technique using IBEM on a wooden engine block, composed of 6 loudspeakers used as noise source simulators. The major advantage of IBEM is the possible estimation of the vibration velocity and the sound intensity right on the surface of an irregularly-shaped source. This allows for very precise noise source location and ranking.

The vibration pattern can be used as a source model in a computer model of a full vehicle and can also be used in a ‘calibration’ procedure of a Finite Element Model of the source structure.

Conclusion


This article reviewed and compared six noise source location techniques. Understanding the concepts of these techniques will lead to choosing the right investigation tool. A new, patented array design was introduced, generating an extremely low Maximum Sidelobe Level when compared to traditional designs. Innovative Sound Source Reconstruction techniques using Inverse Boundary Element Methods have been shown describing automatic regularization of the inverse problem leading to an optimum solution of the discrete ill-posed problem.

Acknowledgements

The authors would like to thank Daimler-Chrysler and Continental for the application examples and some of the results in this article. Special thanks to Jes Sørensen and Abetunji Adebunji from Brüel & Kjær Industrial Marketing for their support. The authors would like to extend very special thanks to the Acoustics Innovation team at Brüel & Kjær, Denmark for their fabulous work, specifically to Finn Nielsen, Jakob Mørkholt, Find Pedersen and Claus Blaabjerg.

References

1. Pierce, A., *Acoustics – Physical Principles and Applications*, second edition Acoustical Society of America, 1989.

2. Kinsler, L. E., *Fundamentals of Acoustics*, Wiley, New York, 2000.
3. Hald, J., "STSF – A Unique Technique for Scan-Based Near-field Acoustic Holography Without Restrictions on Coherences," *Bruel & Kjaer Technical Review*, 1989.
4. Hald, J., "STSF – Practical Instrumentation and Application," *Bruel & Kjaer Technical Review*, 1989.
5. Park, S. H., Kim, Y. H., "An Improved Moving Frame Acoustic Holography for Coherent Acoustic Noise," *Acoustical Society of America*, 1998.
6. Shuhmacher, A., Hald, J., Rasmussen, K. B., Hansen, P. C., "Sound Source Reconstruction Using Inverse Boundary Element Calculations," *Journal of the Acoustical Society of America*.
7. Hald, J., "Non-Stationary STSF," *Bruel & Kjaer Technical Review*, 2000.
8. Johnson, D. H., and Dudgeon, D. E., *Array Signal Processing: Concepts and Techniques*, Prentice Hall, New Jersey, 1993.
9. Hunt, J. T., Knittel, M. R., Barach, D., "Finite Element Approach to Acoustic Radiation from Elastic Structures," *Journal of the Acoustical Society of America*, 1974.
10. Morse, P. M., and Ingard, K. U., *Theoretical Acoustics*, New York, McGraw-Hill, 1968.
11. Abramovitz, M., and Stegun, I. A., *Handbook of Mathematical Functions with Formulas, Graphs and Mathematical Tables*, 9th ed., New York: Dover Publications, 1970.
12. Hwang, J., and Chang, S., "A Retraced Boundary Integral Equation for Exterior Acoustic Problems with Unique Solution for all Wavenumbers," *Journal of the Acoustical Society of America*, 1991.
13. Wrobel, L., and Ferri, A., *The Boundary Element Method – Applications in Thermofluids and Acoustics*, John Wiley and Sons Ltd., 2002.
14. Hansen, P. C., "Rank-Deficient and Discrete Ill-posed Problem," SIAM, Philadelphia, 1998. 

The author can be contacted at: mehdi.batel@bksv.com.